Experimental and numerical investigations of the effects of the spatial distribution of α phase on fracture behavior in hypoeutectic Al-Si alloys

Qian, L.
aDepartment of Production Systems Engineering, Toyohashi University of Technology

Toda, Hiroyuki
Department of Production Systems Engineering, Toyohashi University of Technology

Nishido, Seishi
Aisin Takaoka Co. Ltd.

Kobayashi, T.
Department of Production Systems Engineering, Toyohashi University of Technology

出版情報：Acta Materialia. 54 (18), pp.4881-4893, 2006-10-01. Elsevier
バージョン：
権利関係：

Experimental and numerical investigations of the effects of the spatial distribution of alpha-phase on fracture behavior in hypoeutectic Al-Si alloys

L. Qian[a], H. Toda[a], S. Nishido[b], T. Kobayashi[a]

[a]Department of Production Systems Engineering, Toyohashi University of Technology, Toyohashi 441-8580, Japan
[b]IT Promotion department, Aisin Takaoka Co. Ltd., 1 Tennoh, Takaokashin-machi, Toyota 473-8501, Japan

Keywords: Aluminum alloys; Crack growth; Numerical simulation; Finite-element method (FEM); multiphase microstructure

Abstract

A uniform, fine α-phase microstructure enhances the mechanical properties of Al-Si alloys, however, it is an open question how the α phase affects the crack-growth behavior. This paper addresses the effects of the morphology and distribution of α phase on the fracture behavior in a model dual-phase Al-7%Si alloy with different microstructures. The influences of microstructural factors on crack-growth behavior are examined using in-situ experiments. The results show that a globular α-phase microstructure produces a straight crack-growth path, whereas a dendritic, orientational α-phase microstructure leads to a deflected crack profile. Finite-element modeling is performed to simulate the fracture behavior, and to rationalize the observed phenomena. The near-tip *J*-integral based fracture criterion is used to predict the fracture path. Numerical results indicate that a variation in the morphology and distribution of α phase changes the symmetry and intensity of the near-tip stress, strain and displacement fields due to the strong mismatch in elastic-plastic properties of the α phase and eutectic phase, which have major influences on both crack-growth direction and crack-tip driving force.

1. Introduction

Due to the increasingly widespread applications of cast Al-Si alloys in automotive and aircraft industries, a large volume of research has been conducted to investigate the microstructure-property relationships in such alloys [1-8]. In those studies, the Al-Si alloys were generally produced by mould casting coupled with different cooling rates. A mould-cast hypoeutectic Al-Si alloy is of a dual-phase microstructure, composed of a primary dendrite α phase and an interdendritic eutectic (EU) phase. The α phase is an Al-based solid solution, while the EU phase is an Al matrix dispersed with eutectic Si particles and various kinds of intermetallics. However, the Al-Si alloys produced by a rheocasting technique, one of the presently available casting approaches, show a globular cell α-phase structure other than a dendritic cell microstructure. Such a globular α-phase microstructure provides improved properties such as enhanced ductility, as compared to a dendritic microstructure [9-11]. In contrast to the large volume of research into the damage evolution of Si particles and its deteriorating effects on the deformation behavior and fracture properties mainly in dendrite-structure Al-Si alloys, relatively few studies have been devoted to the effects of the size and shape of α phase on the crack-growth behavior in Al-Si alloys manufactured by different casting techniques.

Indeed, a strong interaction exists between a crack and individual phases in a hypoeutectic Al-Si alloy because of the strong mismatch in elastic and plastic properties between the α phase and the eutectic phase, the spatial distribution of which is believed to affect the symmetry and the intensity of near-tip fields. In the literature [12-20], the effects of the elasticity and plasticity mismatch on fracture behaviors have been extensively investigated in multi-layered materials. The experiments of crack growth in layered materials [12,13] have shown that cracks in the ceramics nearby the interface with the metal were attracted towards the metal layer in systems such as Al_2O_3/Al due to the higher compliance of aluminum, and the cracks were deflected away from the metal layer in systems such as glass/copper since glass was more compliant than copper. In such bimaterial systems, for a crack in a weaker material nearby the interface with a harder material, the crack-tip driving force in terms of the near-tip *J*-integral was reduced, whereas the crack-tip driving force was amplified for a crack in a harder material nearby the interface with a softer material.[16,17]

The specifics of the layered structures are that they have a clear, straight interface or boundary between neighboring constituents with different elastic and plastic properties, while layered materials are just one example of various inhomogeneous materials. The size, shape and distribution of individual constituents with differing elastic and plastic properties are arbitrary and

random in many other engineering materials. In non-layered inhomogeneous materials, crack propagation is not that straightforward. Numerical simulations [21] of the effects of a single α-Al phase in a simplified analytical model demonstrate that both the fracture path and crack driving force are significantly influenced by the presence of α phase, and especially, by the spatial location of the α phase with respect to the crack tip, owing to the fact that a change in the relative location between the α-phase and crack tip varies the near-tip stress-strain fields.

The present work, motivated by the aforementioned experimental and numerical findings, is to investigate and identify the features of fracture behavior in three practical microstructures made of a model Al-7%Si alloy, with different morphologies of α phase and eutectic phase produced by mould casting and by rheocasting. As is known, the effects of individual microstructural features on the damage and fracture of a material are not independent, and the interaction of various structural factors tends to complicate each other; therefore, the damage of Si particles in the eutectic region will be examined as well, since they may directly and significantly affect the fracture properties although it is not the main purpose of this work. First, in-situ observations of crack growth in the three materials are conducted on precracked samples, and the crack-growth trajectories with different features are recognized. Then, typical microstructural features of α phases are extracted and incorporated into finite-element models (FEM) to simulate the fracture behavior, and the local stress, strain and displacement fields are examined to understand the observed behavior micromechanically. This simulation not only helps in identifying and understanding the effects of the spatial distribution of α phase on fracture behavior in hypoeutectic Al-Si alloys, but can be extended to analyze the fracture phenomena in other multiphase materials.

2. Approaches

2.1. Material and experiment

Specimens were cut from the central parts of the ingots of a model Al-7%Si binary alloy, followed by a T6 heat treatment, i.e., solutionized at 535℃ for 4 hours, water quenched, and aged at 180℃ for 3 hours. Two of the ingots were produced by gravity die casting with two types of permanent moulds: cylindrical and ship-shape moulds. The ingot produced by the former mould experienced a low cooling rate, while the latter one was subjected to a high cooling rate, hereafter referred to as materials LC and HC, respectively. The third ingot (hereafter material RE) was prepared by rheocasting. The microstructure of each material after heat treatment was characterized

using an optical microscopy and a scanning electron microscopy. The morphologies of α phase and eutectic Si particles were quantified by examining over 20 view fields at a magnification of 500 ×.

The microstructures of the three materials are shown in Fig. 1, and quantitative measurements are summarized in Table 1. In materials LC and HC, the primary α phase shows a typical dendritic structure. The interdendritic region is filled with the eutectic phase. The size and aspect ratio of Si particles within the eutectic phase, and the size of α phase are significantly larger in LC than in HC. In material RE, the primary α phase takes well-developed sphereodized shape, and the eutectic phase, in which the α phase is embedded, shows a network structure.

Uniaxial tensile properties were measured, and the basic mechanical parameters are shown in Table 2. The basic parameters for Al-12.6Si% alloy and pure aluminum are also included in the table, which were taken from refers [21] and [22], respectively, and will be used as input data for simulation.

Three-point-bend (3PB) specimens with a span of 30 mm, height of 10 mm and width of 2 mm, satisfying the elastic-plastic *J*-integral controlled condition, were adopted for observing crack-growth behavior. A narrow notch was cut, and a fatigue precrack up to the half of the specimen height was produced. The sample surfaces were well polished. The in-situ 3PB experiments were conducted under displacement control on a mini testing stage assembled within the chamber of a SEM. For each material, a pretest was made to record a load-displacement curve during bending. The in-situ tests were then conducted on new specimens. At different loading levels, the loading was interrupted and kept at corresponding displacements, according to the pre-measured load-displacement curve. The surfaces of the samples were examined, crack evolution and the damage of Si particles were evaluated, and the crack paths were identified. The numbers of both intact and damaged particles vs. the distance from the crack tip along the precrack line were counted, and each count was made within a square area of 50×50 μm^2 every 100 μm away from the crack tip along the crack line.

2.2. Simulation methodology

Numerical simulations were conducted using the ANSYS finite-element code. The same geometry of 3PB specimen (Fig. 2) as for the experiment was employed. As we will observe in section 3, the crack-growth path and fracture behavior in material LC are understandable, mainly associated with the damage of Si particles. However, the obvious difference in fracture behavior between HC and RE is not explainable by considering the damage of Si particles only, since Si

particles are quite round and small, and very close in morphology in both materials (Fig. 1 and Table1) and, thus, the extent of the damage of Si particles in HC and LC is similar, as will be evidenced in section 3. As already noticed, the significant difference in the microstructure of the two materials is the morphologies of α phase and EU phase. It is, therefore, quite probable that the morphologies of α phase and EU phase play an important role in controlling crack-growth behavior. Consequently, in this research, we intended to simulate only the fracture behavior in HC and RE for the sake of investigating the effects of the aforementioned two phases. Typical morphologies of α phase and EU phase were sampled, while the existence of specific Si particles was not considered for simplicity. A subdomain of 1000×640 μm^2 was embedded near the crack tip surrounded by a homogeneous region in each model (Fig. 2(a)). The subdomain was composed of α phase and EU phase. The homogeneous region consisted of a uniform Al-7%Si alloy. The interface-oriented problems were ignored, since there is no distinguishable boundary existent between α phase and EU phase in real alloys. The shape of α phase was idealized to be quadratic with a width of ~ 80 μm for HC (Fig. 2(b)), and to be nearly circular with a diameter of ~ 80 μm for RE (Fig. 2(c)). It should be pointed out that the size of α phase in model HC was intentionally designed to be larger than that in the real microstructure (Fig. 1(b)), for the purpose of reducing the total number of elements and shortening the computation time. This is because a tinier microstructure requires finer meshes in the model. Fortunately, this approximation does not affect the prediction of the trends of crack propagation in material HC as demonstrated in Section 4.

Multiple data points of true stresses and logarithmic strains of the uniform Al-7%Si alloy and its two constituting phases were input into FEM code. The basic data for the uniform Al-7%Si alloy were taken from material HC. Note that the EU phase in the Al-7%Si alloy is equivalent to an Al-12.6%Si alloy, while the α phase consists of Al plus 1% Si in solution. The stress-strain data for the EU phase were thus taken from the Al-12%Si alloy, which was cast using the same processing route as material HC [21]; and the data of 99.99% Al, taken from refer [22], were used to approximate that of the α phase. Assume that the above approximation has only a minor effect on the general behavior of the simulated materials.

An incremental plasticity theory was used to simulate the elastic-plastic behavior. The materials were assumed to deform plastically, obeying von Mises yielding surface. An isotropic hardening was presumed, and the plastic-strain increments were governed by the Prandtl-Reuss associated flow rule. Two-dimensional, plane-strain, elastic-plastic finite elements were used, with about 11200 elements in each model. The mesh was gradually decreased from the outer to the tip region of the crack, with a minimum size of 3μm near the tip. Both lower supporting points of the

specimen were fixed. The load was applied at the upper midpoint under displacement control. For each step of crack advance, the displacement was increased incrementally up to an applied displacement of ~ 0.4 mm, which is close to the crack-initiation point. A Newton-Raphson iteration algorithm was implemented to solve the nonlinear finite-element equations. The convergence of the solutions was checked after each loading increment during computation.

One important issue involved with crack-growth simulation is how to predict crack-growth direction. It is known that the crack growth in elastic-plastic multiphase materials is not in a self-similar style, but in a mixed mode.[23,24] Various criteria have been proposed for predicting the critical state of crack growth and crack-growth direction under mixed-mode loading. Among these criteria are the maximum hoop stress criterion, [25] the minimum strain energy density criterion, [26] and the maximum strain energy release rate criterion [27]. However, there is no a single criterion applicable to all materials or to all loading conditions. As discussed and verified in [21], the *J*-integral-based criterion is more applicable to the present materials. Based on this criterion, the crack-growth angle is determined by [28,29]

$$\theta = \tan^{-1}(J_y / J_x), \qquad (1)$$

where J_x and J_y are the components in the directions parallel and perpendicular to the mode-I crack, respectively, and evaluated numerically along a contour path Γ surrounding the crack tip as follows: [30]

$$J_k = \int_{\Gamma} \left[w n_k - \sigma_{ij} \frac{\partial u_j}{\partial k} n_i \right] d\Gamma, \qquad k = x \text{ or } y \qquad (2)$$

The origin of the coordinate system is set at the crack tip, x axis is on the crack line, and y axis is vertical to the crack line. The term w is the strain energy density, n_i is the Cartesian component of the unit outward normal vector to the contour, σ_{ij} and u_j are the Cartesian components of the stress tensor and the displacement vector. As required by the *J*-integral-based fracture mechanics, the *J*-integral path should be chosen to pass through a uniform region and, thus, the calculated *J*-integral value shows path independence. In multiphase materials, however, *J*-integral is path dependent on the whole. Nevertheless, when an inner path is taken and when it passes through a single phase only, an almost identical *J*-integral value can be obtained regardless of the path selection, which gives the crack-tip driving force (hereafter J_{tip}), and reflects the effect of second phases on the driving force [15-17,21,31,32]. On the other hand, the *J*-integral path cannot be too near the crack tip when considering the calculation accuracy. In the present specific models, the integral path was taken along a circular contour of r = 20 μm centered at the crack tip, which has been confirmed to be reasonable [21]. The crack-growth direction was, thus, predicted according to

Eq. 1. The distance of one-step crack growth was taken to be 25 μm (as substantiated to be appropriate in [21]), but occasionally adjusted to be more or less than this value, in order that the new crack tip was not located at or so close to the boundary between α phase and EU phase and, thus, the *J*-integral path always passed through a uniform region. The continuous crack-growth behavior was, hence, simulated by repeating the aforementioned processes using a step-by-step procedure [21].

3. Observed fracture behavior

The observed crack paths and near-tip damaged microstructures after a longer crack extension for each material are shown in Figs. 3 and 4. In LC, the plastic deformation is confined in the α phase very close to the crack-tip region (Fig. 3a), Si particles in EU phase near in front of the precrack tip are severely damaged mainly in the form of breakage, and microcracks are generated at the damaged particles (Fig. 4a). These microcracks easily grow into the matrix and connect with other microcracks. With further increasing the load, the microcracks generated in one EU phase link to those in neighboring EU phases, leading to the fracture of α phase between two adjacent EU phases. The connected microcracks join to the main crack, leading to the intermittent crack extension. In HC and RE, plastic deformation occurs in both the α phase and EU phase, however, there are apparently more and coarser slip bands in the α-phase (Fig. 4b and c); Si particles in the EU phase are damaged mainly by particle/matrix debonding, which leads to void initiation, although cracking of particles are also visible in the two materials. Both the plastic zone and particles' damage zone span a much larger area in front of the crack tip in either HC or RE than in LC. Unlike in LC, in which the extension of the main crack is caused by the connection of the damage in neighboring EU phases before fracturing the α phase between them, in HC and RE, however, the crack penetrates one α phase followed by passing through one EU phase consecutively, and vice versa. It is particularly note worthy that the crack morphology in HC is different from that in RE. In the former material, the crack frequently deflects, and at times, deviates largely from the mode-I crack direction (Fig. 3b), whereas in RE the crack extends almost in a straight-line fashion, passing through both the EU phase and α phase continuously whichever the crack encounters (Fig. 3c).

The accumulated damage ratios of Si particles, determined as the number of all the damaged particles divided by the number of all the intact and damaged particles, are plotted in Fig. 5(a) and (b), as a function of distance from the crack tip r, and normalized distance $r\sigma_0/J$, respectively. Note

that the particles' damage zone sizes, r_d, of HC and RE, ~ 1 mm, are much larger that that of LC, ~ 0.2 mm (Fig. 5a). However, the damage ratios of Si particles in all the three materials fall almost within the normalized distance of about 0.9, i.e., $r_d \approx 0.9\ J/\sigma_0$, which is about three times the crack-tip opening displacement (CTOD), δt, when $\delta t = d_n \cdot J / \sigma_0$ is applied. Here, σ_0 is the yield stress, J is the applied J-integral, and d_n is a dimensionless constant, which is ~ 0.3 for the three materials with a hardening exponent of n ≈ 5 according to Shin [33]. These results are not unreasonable. According to [34, 35], the stress reaches a peak at approximately two times CTOD when yielding occurs and, thus, microcrack initiation typically occurs at the particles of $r_d \approx 2\delta t$ from the crack tip. However, the damage zone size of particles is more or less larger than $2\delta t$, depending on the in-situ fracture strength of particles or the particle/matrix interfacial strength, and the yielding behavior of the matrix surrounding the particles.

When the in-situ fracture strength σ_f is exceeded by the internal stress of Si particles σ_p, the cracking of particles will occur. σ_f depends on various factors, such as the size, aspect ratio and volume fraction of the particles.[36] Particles with larger size or larger aspect ratio will fracture at smaller σ_f. For an approximate estimation of σ_f, Si particles are assumed to be spherical with an average diameter, D, as determined in Table 1. Thus, σ_f can be approximated by [37,38]

$$\sigma_f = \sqrt{\pi E \gamma_s / D} \qquad (3)$$

where γ_s is the specific surface energy for Si, 1.0 J/m^2, and E is the Young's modulus for Si, 161 GPa.[39]. The estimated mean value of σ_f for LC is 178 MPa, much lower than those for HC and RE, 360 and 397 MPa, respectively. Considering the larger aspect ratio of Si in LC, the σ_f value should be even lower. Therefore, the particles in LC are broken much easily and severely, and the crack tends to follow the cracked particles. Conversely, since the mean σ_f values for HC and RE are much higher, fracturing of particles becomes difficult. The probability of particle fracturing will be increased only when the internal stress of particles is raised by further applying the load; however, debonding of the particle/matrix interface will occur when the particle stress is able to exceed the interfacial strength σ_{int} at a higher load.[40] Concurrently, a larger crack opening, plastic zone and particles' damage zone take place in front of the crack tip; and the crack paths in HC and RE do not necessarily follow the damaged particles since the damage of particles in the two materials is not so severe as in LC.

4. Simulated fracture behavior

As we have identified that the fracture behavior of material LC is mainly affected by the damage of Si particles, associated with their larger size and aspect ratio. However, the observed difference in fracture path and crack-growth behavior between HC and RE is not accountable by considering the damage of Si particles solely, since Si particles are damaged to a similarly less extent in both HC and RE. According to the following analyses, we believe that the difference in the spatial distribution of α phase (and EU phase as well) should be responsible for the different fracture behavior in the two materials.

4.1. Crack growth path

Fig. 6(a) and (b) shows the simulated fracture path and deflection angles, respectively, in model HC. The fracture path is superimposed upon the microstructure, to illustrate its relationship with different phases. The deflection angle, θ, as exemplified in the inset in Fig. 6(b), is plotted as a function of distance from the precrack tip on the precrack line. There are two colonies (colonies A and B) of dendritic cells in HC, each having a different secondary dendrite arm orientation with respect to the precrack line. The initial crack tip is located in the slanted quadratic α phase in colony A. At the very beginning, the crack at location 1 grows downwards, with a deflection angle of about -10^0. Then, the crack deviates more away from the mode-I crack direction with deflection angles between $-20 \sim -40^0$, until it reaches colony B. Afterwards, the crack returns to near mode-I direction at location 11. Interestingly, after a short mode-I crack growth, the crack rotates upwards at location 13, and penetrates the α phase and EU phase at deflection angles of $15 \sim 20^0$ through the remaining propagation steps.

Fig. 7 (a) and (b) shows the simulated fracture path and deflection angles, respectively, in model RE. A completely different crack path is observable, when compared with that in model HC. The deflection angles at various crack locations are almost within $-10 \sim 6^0$ from the precrack line. The overall crack profile shows a nearly straight line, approximating the precrack line, regardless of passing through either α phase or EU phase.

4.2. Symmetry of near-tip fields

By comparison with the observed fracture paths in section 3, we can see similarities between the simulations and the experiments. These results, hence, indicate that the different crack profiles observed in HC and RE are, to a larger extent, attributed to the difference in the morphology and

distribution of α phase in the two materials. As has been recognized in the literature [16-20], non-symmetrical stress-strain fields exist near the crack tip in inhomogeneous materials due to the mismatch in elastic and plastic properties, which cause the near-tip mixed-mode loading; and the magnitude and sign of the mode-II loading component determine the crack deflection and fracture path. We examined the angular distributions of various fields along a circular contour close to the crack tip with r = 20 μm, which would provide a direct picture of such symmetry of fields in each model. The near-tip angular variations of stresses (σ_{yy} and σ_{xy}), and plastic strains (ε^{p}_{yy} and ε^{p}_{xy}) at several representative crack tip locations are shown in Figs. 8 and 9, respectively. The symmetrically distributed fields of the uniform Al-7%Si alloy are also shown for a comparative purpose. We can see a much higher degree of symmetry of the near-tip fields in model RE than in model HC, quite resembling that of the uniform material. This is especially apparent by examining the shear stress and shear strain fields.

The contour patterns of the stress-strain fields ahead of the crack tip, as typically shown in Figs. 10 and 11, would assist in further understanding the relationship among the microstructure, near-tip fields and fracture behavior. Note that that high stresses are concentrated to the EU-phase region, and high strains are confined to the soft α-phase region in both models, due to the large difference in the yield strength between the α phase and EU phase; and the contour patterns are completely different between the two models. In RE, the contour patterns are uniformly distributed, which is closely related to the uniform globular α-phase microstructure. As a result, a high degree of symmetry of the near-tip fields occurs on both sides of the crack tip. It follows that the crack tends to be attracted or repelled by the two phases on one side of the crack, and to be nearly equally attracted or repelled by the two phases on the other side. That is, the offsetting effect of the uniformly and symmetrically distributed network microstructure leads to a straight crack path. In HC, however, the contour patterns show obvious directional distribution, which is closely related to the quadratic, dendritic α-phase microstructure. Such directional plastic flow along the quadratic α-phase brings about a low degree of symmetry of the near-tip fields. It follows that the crack tends to be attracted/repelled by the α phases/EU phases on one side of the crack, but to be unevenly attracted/repelled by the two phases on the other side. Hence, a deflected crack profile results from such asymmetrical near-tip fields.

4.3. Crack driving force

The crack driving force was evaluated by examining the normalized contour J-integral, J_{tip}/J_{far},

versus the crack tip location. The near-tip *J*-integral, J_{tip}, is evaluated along a contour lying in a single phase within the crack-tip region; the far-field *J*-integral, J_{far}, is calculated along a contour in the region far outside the subdomain in the models. The difference between the *J*-integrals J_{tip} and J_{far} reflects the microstructural effects on the driving force [15-17, 21]. The ratio $J_{tip}/J_{far} > 1$ implies an amplification of the driving force, while the ratio < 1 implies a shielding effect. The results are shown in Fig. 6(c) and 7(c) for models HC and RE, respectively, under a given applied displacement of 0.4 mm. Note that the normalized driving force changes frequently from position to position, surrounding the line of $J_{tip}/J_{far} = 1$. Both amplification and shielding effects occur in the two models, depending on the crack tip location. In the EU phase, the driving force can be amplified (as circled by solid lines) and can be shielded as well (as circled by dashed lines); in the α phase, both amplification and shielding effects can occur, too. These results indicate that the amplification or shielding effect depends on the crack-tip material environment, i.e., the phase distribution around the crack tip regardless of whether the crack tip is located in the α phase or in the EU phase.

4.4. Intensity of near-tip fields

To better understand the variations of near-tip fields and their effects on the driving force with crack tip locations, we re-examined the near-tip fields in both models (Figs. 8 and 9). By comparing different crack-tip locations, we note that the magnitude of driving force is not separately dictated by the intensity of either near-tip stress fields or near-tip strain fields. This is due to the fact that the driving force in terms of the *J*-integral is a function of near-tip stress, strain and displacement fields along the integral contour according to Eq. (1), unlike either in the stress-controlled fracture where an amplification of driving force is owing to the increase in the intensity of stress fields, or in the strain-controlled fracture where an enhanced driving force is a result of the increased intensity of strain fields. We can further note that, with the variation of crack-tip location in each model, the spatial distribution of individual phases near the crack tip is different (though the difference does not appear to be so large in some cases), accordingly, the intensity of near-tip fields of stresses, strains or displacement varies with the crack-tip location, which causes the alteration in driving force.

The above analyses were based on two typical cases of α phase arrangement only, though there exist other complicated spatial distributions of such phases in real materials in a statistical point of view, especially when 3D microstructures are considered. [23,24,41-43] In addition, the damage of

Si particles was not considered in the models, although it does affect directly the fracture behavior. Thus, more systematic investigations are needed for a complete interpretation of fracture problems, for example, including the damage of Si particles, statistical considerations of local fracture events and 3D microstructural information in the models. However, the present work does not lose its implications in enabling us to recognize and understand micromechanically the effects of the spatial distribution of α phase (and EU phase as well) on the fracture behavior not only in hypoeutectic Al-Si alloys but also in other multiphase materials.

5. Conclusions

The damage and fracture behavior in a model Al-7%Si alloy have been investigated using in-situ experiments and finite-element modeling. In materials LC and HC, which were produced by mould casting with a low cooling rate and a high cooling rate, respectively, the microstructures consist of dendritic α phase and interdendritic eutectic (EU) phase dispersed with Si particles; the size and aspect ratio of eutectic Si particles are significantly larger, and the secondary dendrite arm spacing is also appreciably larger in LC than in HC. In material RE, which was prepared by rheocasting, the microstructure consists of uniformly-distributed globular α phase embedded in the network of eutectic phase; the Si particles are small, almost of the same size as in HC. The following conclusions are reached.

1. In material LC, crack path seems to be mainly associated with the damage of Si particles, since the particles are large in both size and aspect ratio, and easy to break. Microcracks are first initiated at the severely damaged Si particles, then link to those in neighboring EU phases, which leads to the fracture of the α phase between adjacent EU phases, and finally join to the main crack. In materials HC and RE, Si particles are small, and the fracture behavior of the two materials is, to a similarly less extent, influenced by the damage of Si particles. However, the crack in HC takes a deflected morphology, whereas in RE it grows almost in a straight-line fashion, passing through both the α phase and EU phase continuously. The difference in crack path between HC and RE cannot be interpreted by considering only the extent of the damage of Si particles, but is believed to be due to the different morphology and distribution of α phase in the two materials.

2. Numerical simulations based on the elastic-plastic finite element modeling and the near-tip *J*-integral criterion have reproduced a deflected crack profile in the model with quadratic α phases, and a nearly straight crack path in the model with globular α phases. The simulated crack profiles

resemble the experimentally observed crack paths in materials HC and RE, respectively, confirming the significant role of the spatial distribution of α phase in controlling crack-growth behavior in Al-Si alloys.

3. Examination of the near-tip fields indicates that the morphology and distribution of α phase affect the symmetry and intensity of the near-tip fields due to the large mismatch in elastic-plastic properties of the α phase and EU phase, therefore influencing the crack-growth behavior. A high degree of symmetry of the near-tip fields occurs in model RE, leading to a straight crack-growth path. However, a low degree of symmetry of the near-tip fields takes place in model HC, leading to a deflected crack profile.

4. The driving force in terms of the *J*-integral is not governed by a single mechanical quantity but by a combination of the near-tip fields of stress, strain and displacement. The magnitude of near-tip fields varies with the crack tip location, due to the variation of near-tip material environment (orientation and distance of the individual constituents with respect to the crack tip), which causes the alteration of crack driving force.

Acknowledgements

L. Q. gratefully acknowledges the Japanese Society for the Promotion of Science (JSPS) for the financial support through JSPS fellowship, and the Grant-in-aid for Scientific Research through subject No. 16･04370. The support from the Light Metal Educational Foundation to H. T. is also gratefully acknowledged.

References

[1] Fat-Halla N. J Mater Sci 1987;22:1013-1018.

[2] Lee FT, Major JF, Samuel FH. Fat Fract Eng Mater Struct 1995;18:385-96.

[3]Horstemeyer MF. From Atoms to Autos, A New Design Paradigm Using Microstructure-Property Modeling: Part 1: Monotonic Loading Conditions. Sandia National Laboratories (California), 2001.

[4] Nishido S, Kaneso M, Kobayashi T, Toda H. Int J Cast Metals Res 2004;17:1-6.

[5] Oswalt KJ, Misra MS. AFS Trans 1980;88:845-62.

[6] Davis JR. Aluminum and aluminum alloys. Materials Park (OH): ASM International, 1993. p.220.

[7] Yeh J-W, Liu WP. Metall Mater Trans A 1996;27:3558-68.

[8] Hafiz MF, Kobayashi T. J Mater Sci 1996;31:6195-200.

[9] Surey M. Thixocasting of aluminum alloys: from microstructure in the semi-solid state to mechanical properties. in: Kobayashi T, Murakami Y, Sato T, Kumai S, editors. Proc. of ICAA-6. The Japan Institute of Light Metals (Tokyo), 1998. p.51-62.

[10] Shibata R, Kareuchi T, Soba T, Izaka I. New semi-liquid metal casting process. Proc. 4th Int Conf on the semi-solid processing of alloys and compsites. The University of Sheffield (Sheffield), 1996. p.19-21.

[11] Toda H, Kobayashi T, Noguch T, Wade N, Ahn, H-K, Yu C-H. Proc. EUROMAT 2001, CD-ROM, 2001.

[12] McNaney JM, Cannon RM, Ritchie RO. Acta Mater 1996;44:4713-28.

[13] McNaney JM, Cannon RM, Ritchie RO. Int J Fract 1994;66(3):227-40.

[14] Kolednik O. Int J Solids Struct 2000;37:781-808.

[15] Simha NK, Fischer FD, Kolednik O, Chen CR. J Mech Phys Solids, 2003;51:209-40.

[16] Sugimura Y., Lim PG, Shih CF, Suresh S. Acta Metall Mater 1995;43:1157-69.

[17] Kim AS, Suresh S, Shin CF. Int J Sol Struct 1997;34:3415-32.

[18] Suresh S, Sugimura Y, Ogawa T. Scr Metall Mater 1993;29:237-42.

[19] Suresh S, Sugimura Y, Tschegg EK. Scr Metall Mater 1992;27:1189-94.

[20] Liu B, Kimoto H, Kitagawa H. Eng Fract Mech 1996;53:607-23.

[21] Qian L, Toda H, Nishido S, Akahori T, Niinomi M, Kobayashi T. Metall Mater Trans 2005;36A:2979-92.

[22] Krauss G. Deformation, Processing and Structure. Metals Park (OH): ASM, 1982. p.91.

[23] Toda H, Sinclair I, Buffière J-Y, Maire E, Connolley T, Joyce M, Khor KH, Gregson P. Phil Mag 2003;83:2429-48.

[24] Toda H, Sinclair I, Buffière J-Y, Maire E, Khor KH, Gregson P, Kobayashi T. Acta Mater 2004;52:1305-17.

[25] Erdogan F, Sih GC. J Basic Engng, ASME 1963;85:519-27.

[26] Sih GC, Madenci E. Eng Fracture Mech 1983;18:1159-71.

[27] Wu CH. Int Appl Mech. 1978;45:553-8.

[28] Hussain MA, Pu SL, Underwood J. Fracture Analysis, ASTM STP560, ASTM, 1974. p.2-28.

[29] Riddle RA, Streit RD, Finnie I. Fracture Mechanics, 8th symposium, ASTM STP 945, edited by Read DT, Reed RP. ASTM (Philadelphia), 1988. p.118-33.

[30] Budiansky B, Rice JR. J Appl Mech 1973;40:201-3.

[31] Anderson TL. Fracture Mechanics: fundamentals and applications. Boca Raton (FL): CRC press, 1995. p.578.

[32] Moran B, Shih CF. Eng Fract Mech 1987;27:615-42.

[33] C.F.Shih. Report MRL E-147, Brown University, 1983.

[34] McMeeking RM, Parks DM. Elastic-plastic Fracture, ASTM STP 668, edited by Landes JD, Begley JA, Clarke GA, ASTM (Philadephia), 1979. p.175-94.

[35] Anderson TL. Fracture Mechanics: fundamentals and applications. Boca Raton (FL): CRC press, 1995. p.280.

[36] Brechet Y, Embury JD, Tao S, Luo L. Acta Metall Mater 1991;39:1781-6.

[37] Curry DA, Knott JF. Met Sci 1979;13:341-5

[38] Lee FT, Major JF, Samuel FH. Metall Mater Trans 1995;26A:1553-70.

[39] Cook RF. J Mater Sci 2006;41:841-72.

[40] Argon AS, Im J, and Safoglu R. Metall Trans 1975;6 A:825-37.

[41] Qian L, Toda H, Uesugi K, Kobayashi T, Ohgaki T, Kobayahsi M. Appl Phys Lett 2005;87:241907.

[41] Kulkarni A, Herman H, DeCarlo F, Subramanian R. Metall Mater Trans A 2004;35:1945.

[43] Stock SR. Int Mater Rev 1999;44:141.

Figure 1

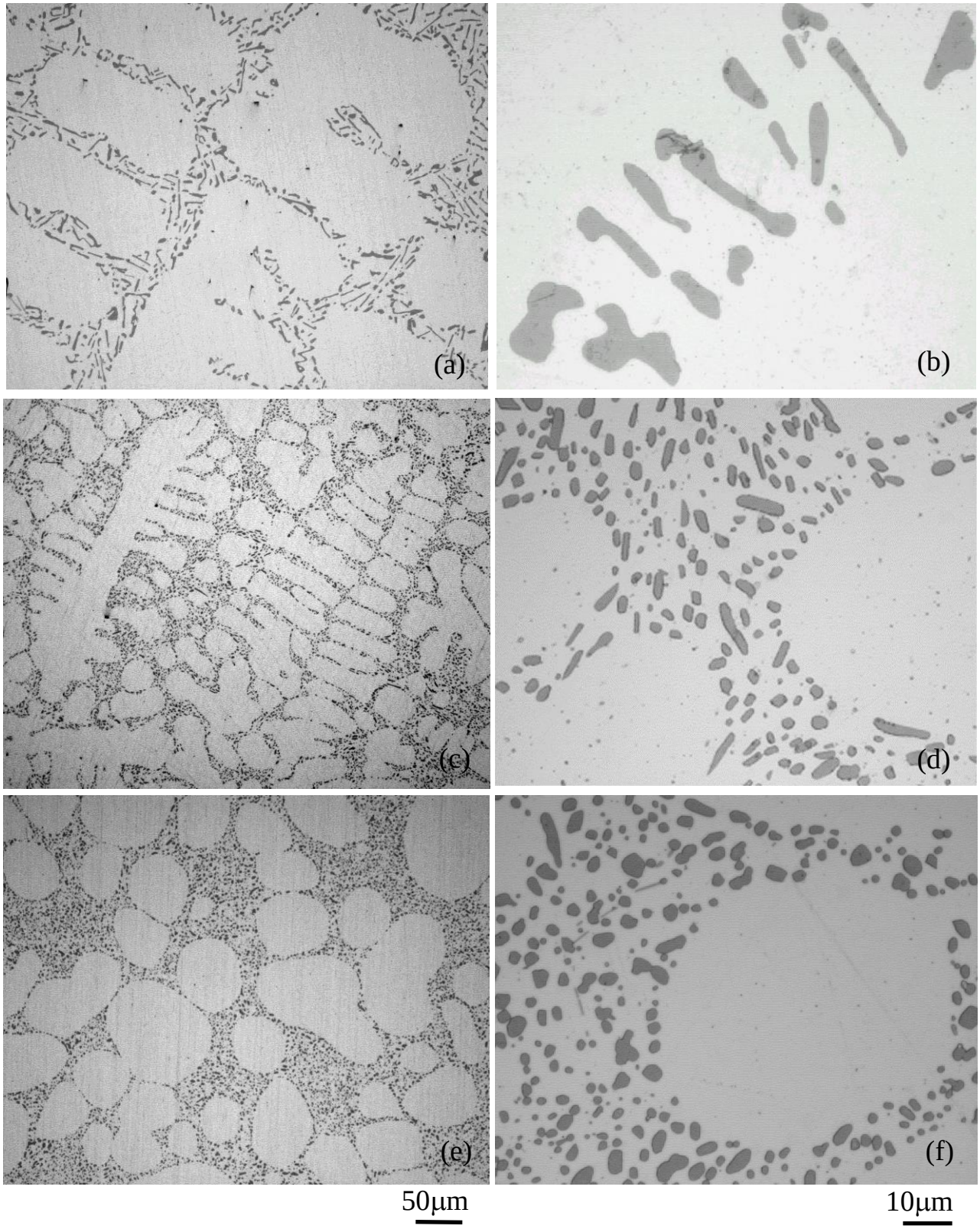

Fig.1 Optical microstructures of materials LC (a and b); HC (c and d); and RE (e and f).

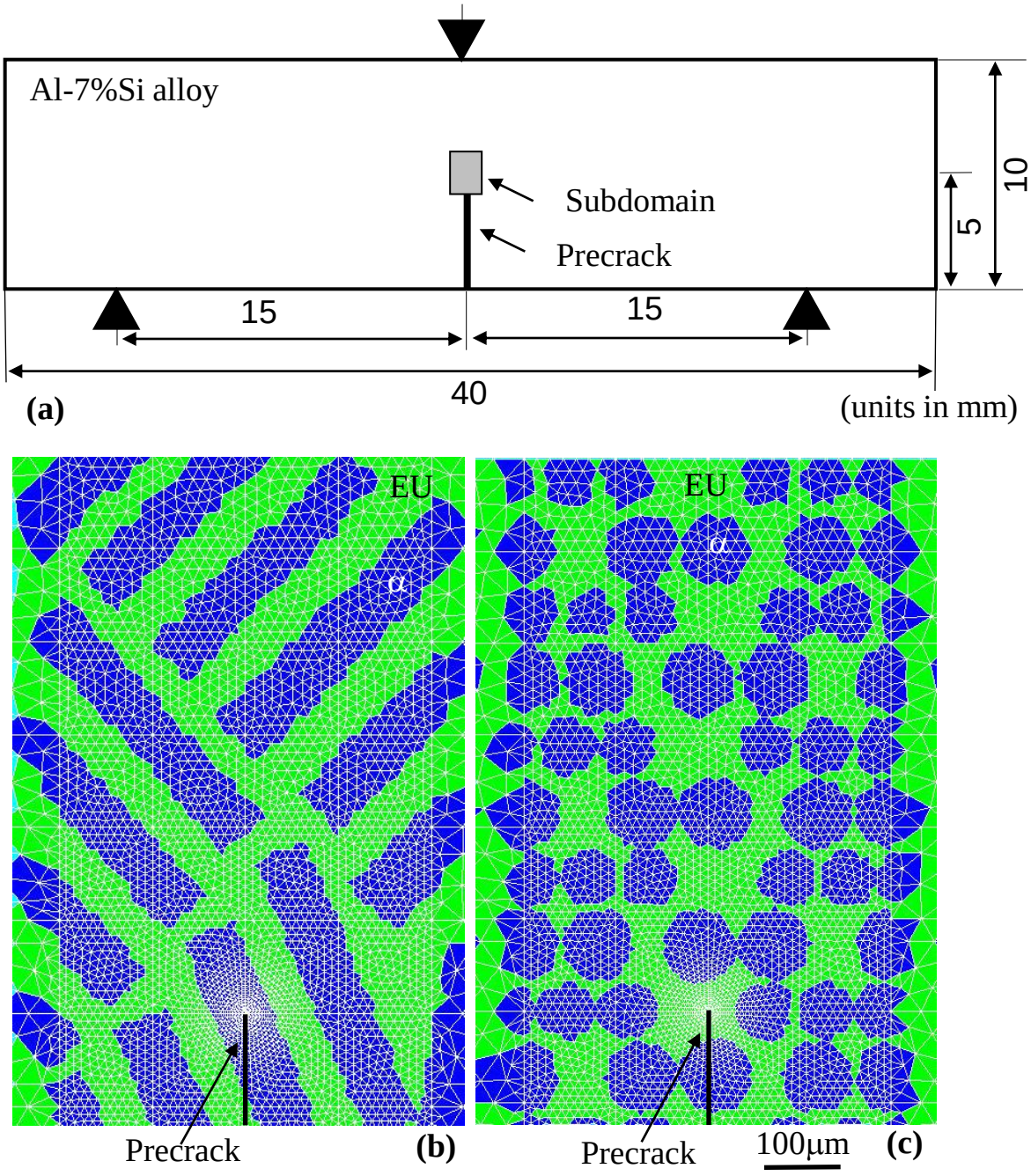

Fig.2 (a) Specimen configuration; (b) and (c) element meshes around the precrack tip within the subdomain indicated in (a) for models HC and RE, respectively. The α phases are quadratic in HC, and nearly circular in RE.

Figure 3

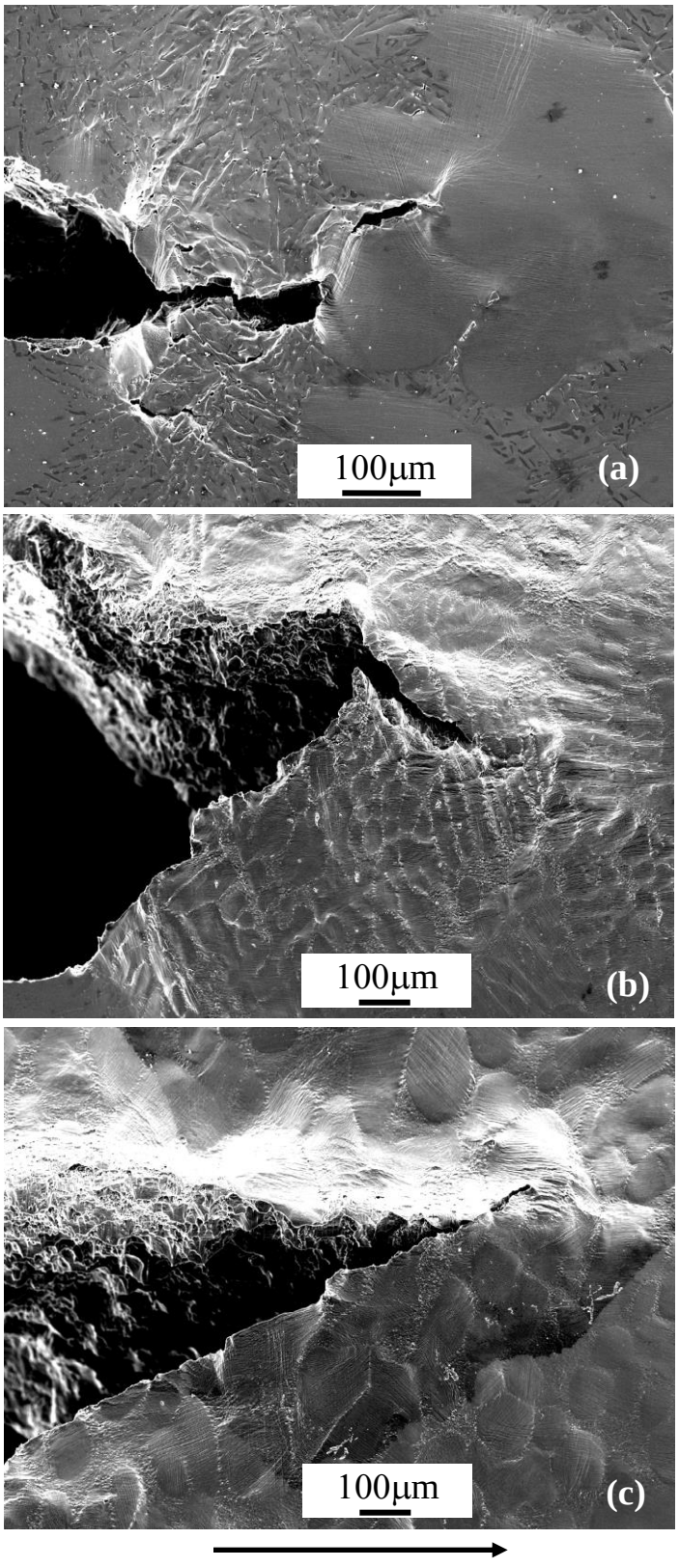

Fig.3 Crack profiles after a long crack extension for materials (a) LC, (b) HC and (c) RE.

Figure 4

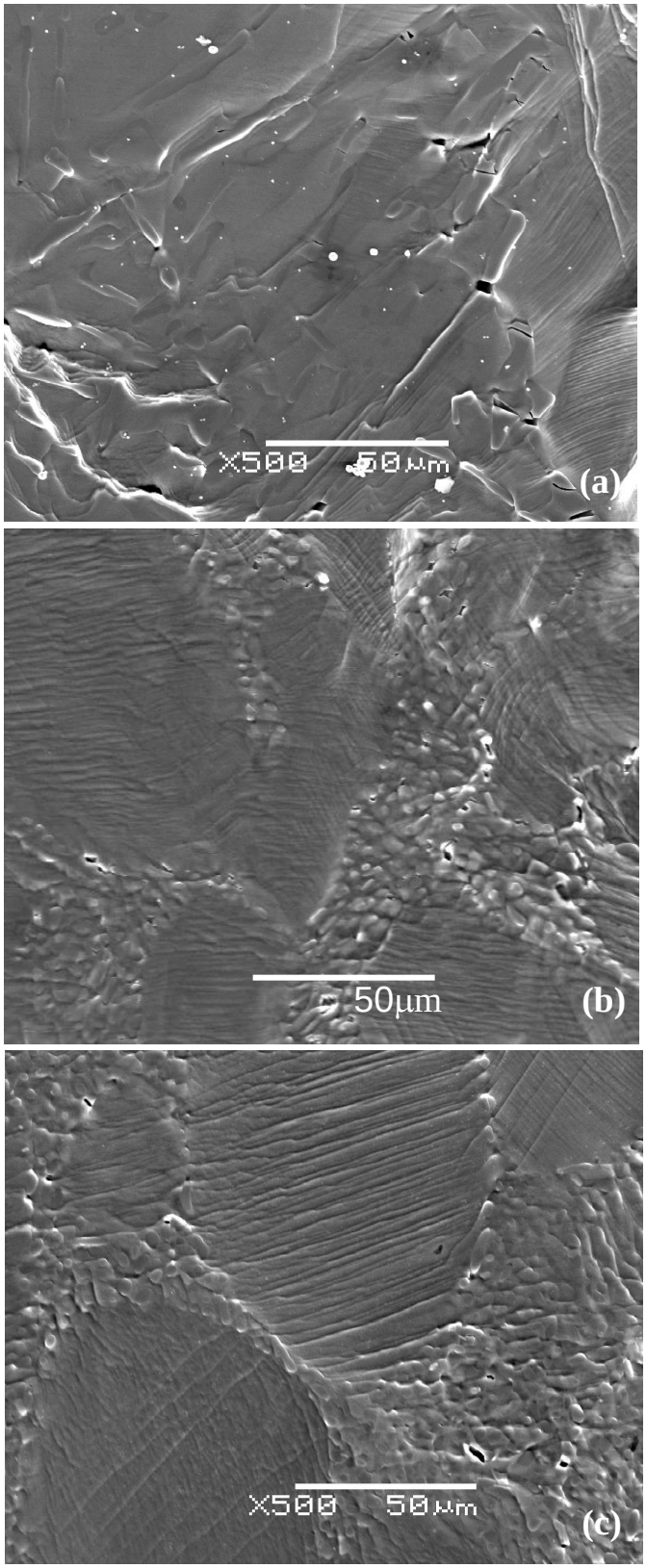

Fig.4 Near-tip damaged microstructures for materials (a) LC, (b) HC and (c) RE, showing severe plastic deformation in α phase and particles' damage in EU phase.

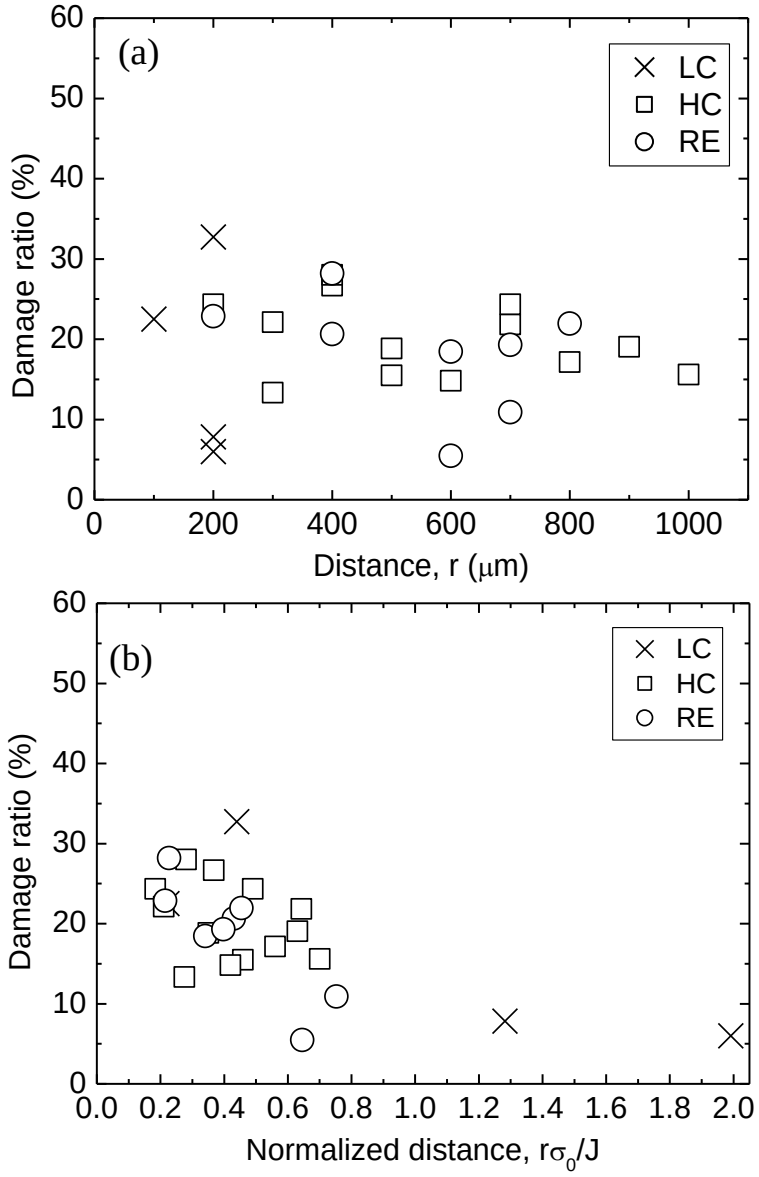

Fig.5 Damage ratios of Si particles as a function of distance from crack tip r (a), and normalized distance rJ/σ_0 (b) for materials LC, HC and RE.

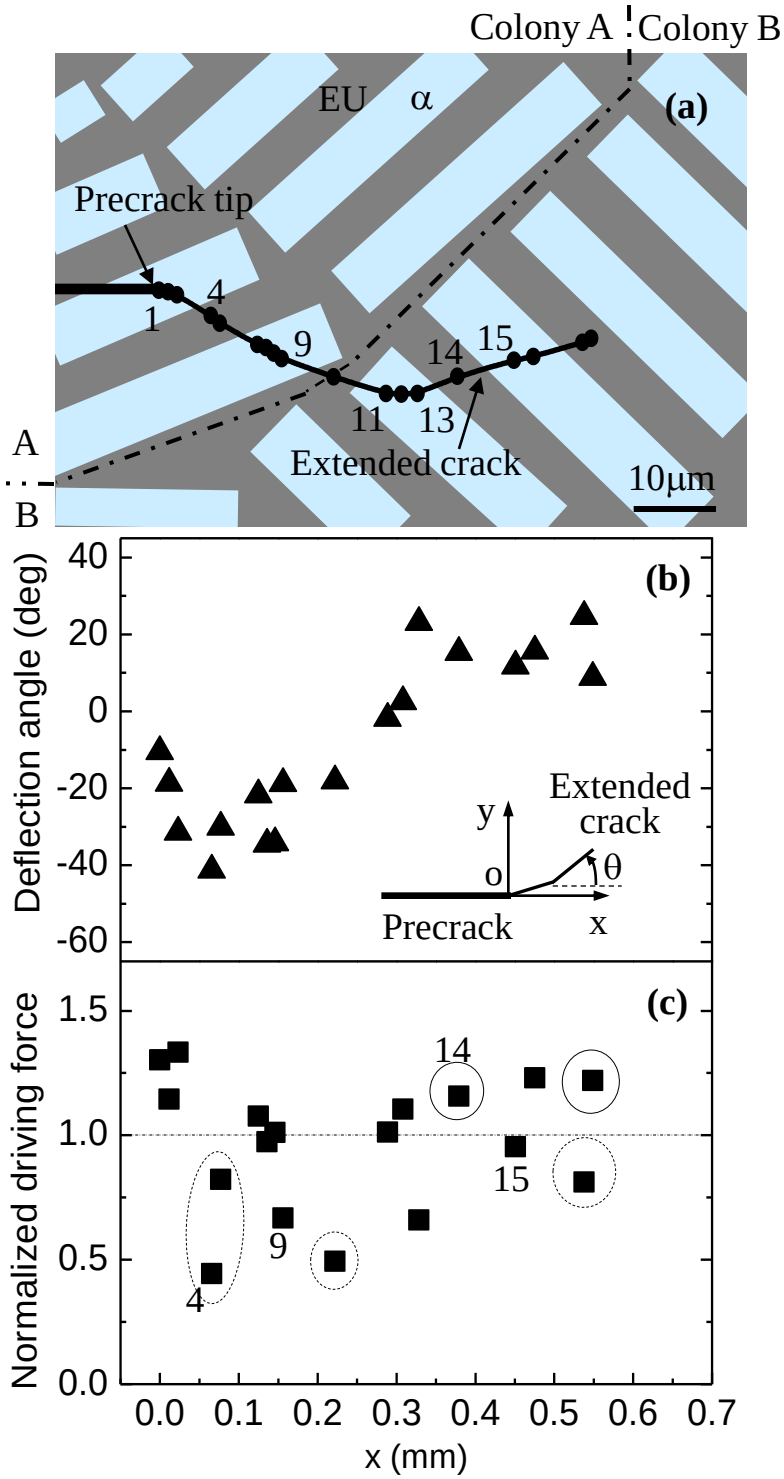

Fig.6 (a) Simulated crack-growth path in relation to the constituting phases, (b) crack-deflection angle θ, and (c) normalized driving force J_{tip}/J_{far} vs. crack-tip location for model HC. The circles indicate that the crack tip is located in EU region.

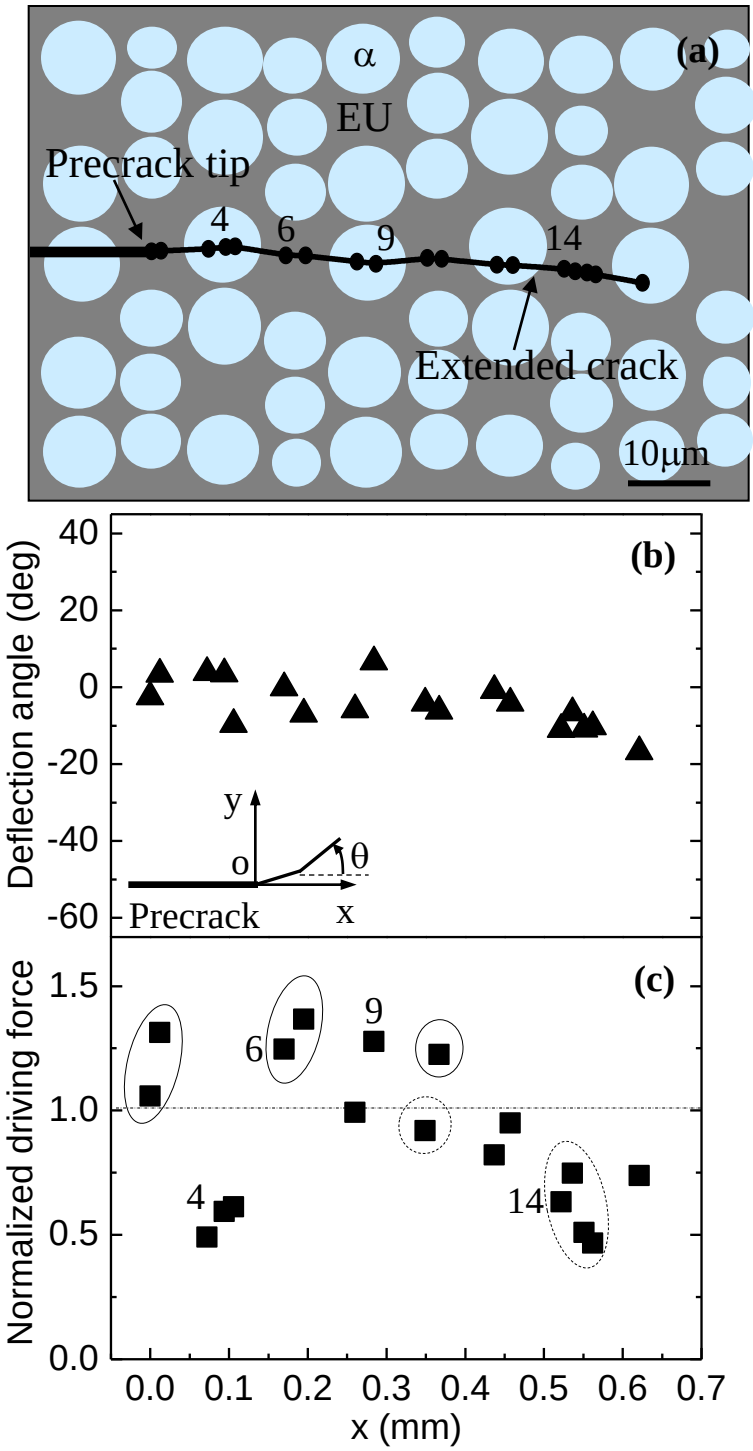

Fig.7 (a) Simulated crack-growth path in relation to the constituting phases, (b) crack-deflection angle θ, and (c) normalized driving force J_{tip}/J_{far} vs. crack-tip location for model RE. The circles indicate that the crack tip is located in EU region.

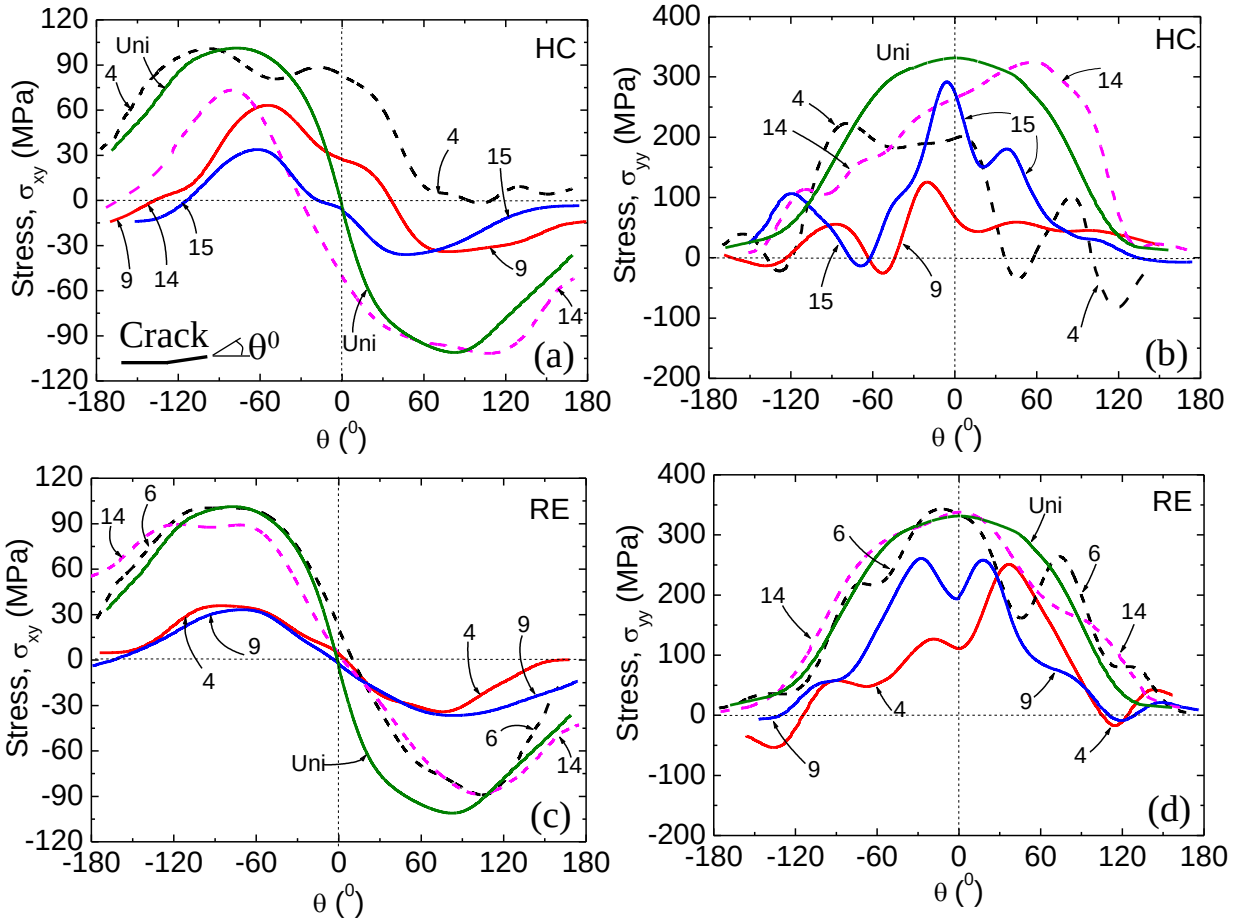

Fig.8 Circumferential variations of stresses σ_{xy} and σ_{yy} for models HC (a and b) and RE (c and d). The crack-tip fields of the uniform Al-7%Si alloy are also shown. The numbers correspond to the crack-tip locations indicated in Figs. 5 and 6.

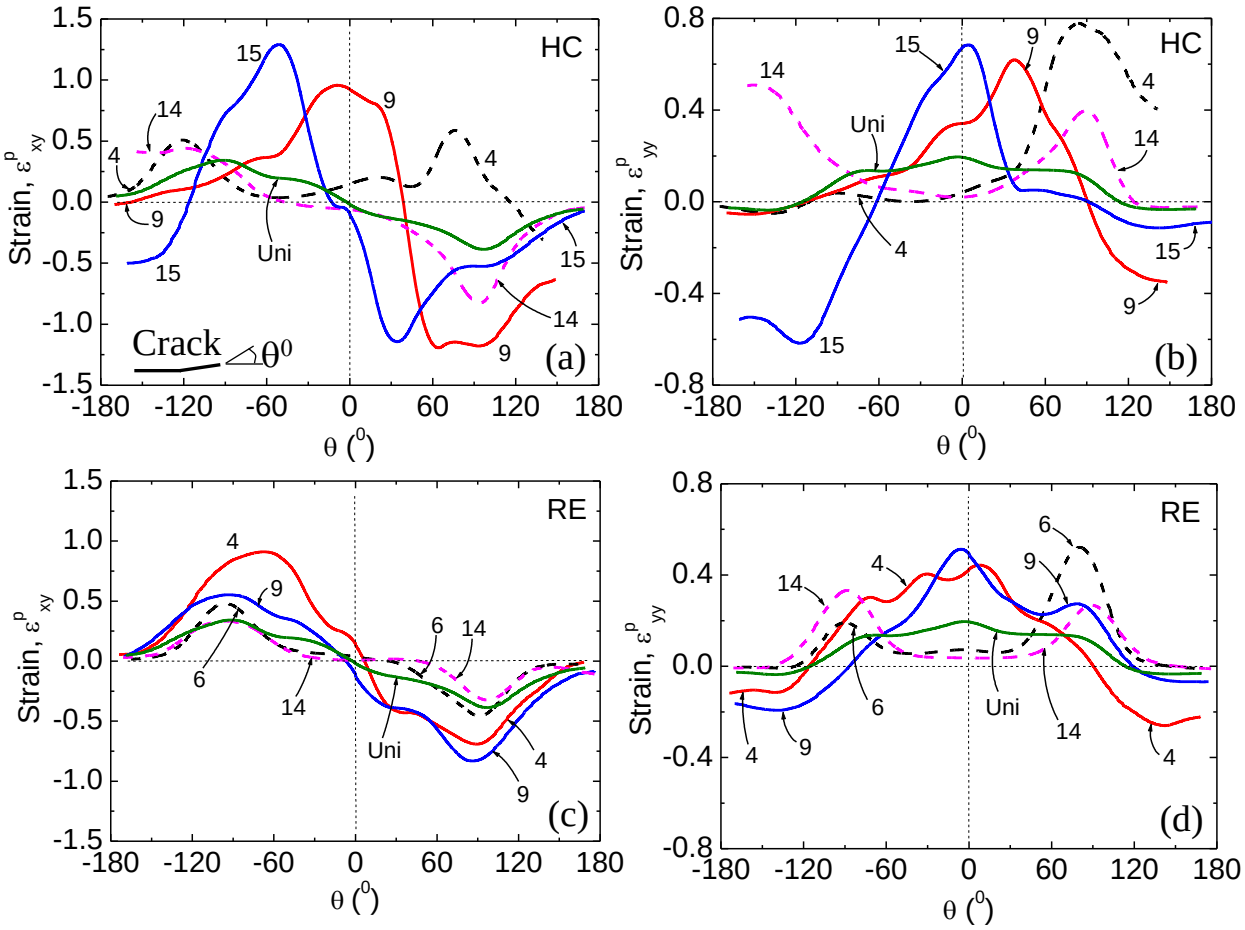

Fig.9 Circumferential variations of plastic strains ε^p_{xy} and ε^p_{yy} for models HC (a and b) and RE (c and d). The crack-tip fields of the uniform Al-7%Si alloy are also shown. The numbers correspond to the crack-tip locations indicated in Figs. 5 and 6,

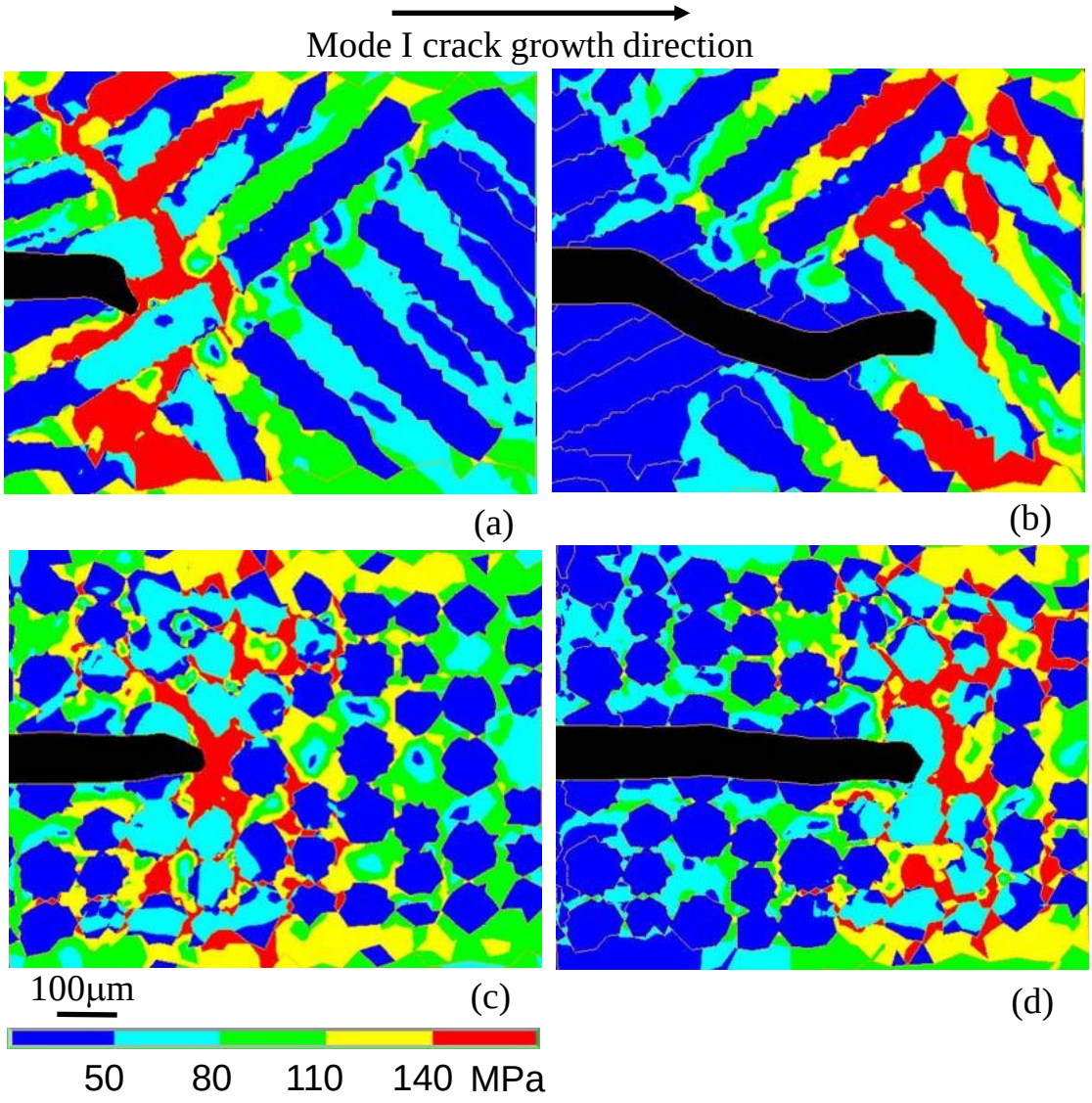

Fig.10 Simulated crack growth paths at two crack lengths, superimposed on equivalent stress contours for models HC (a and b); and RE (c and d).

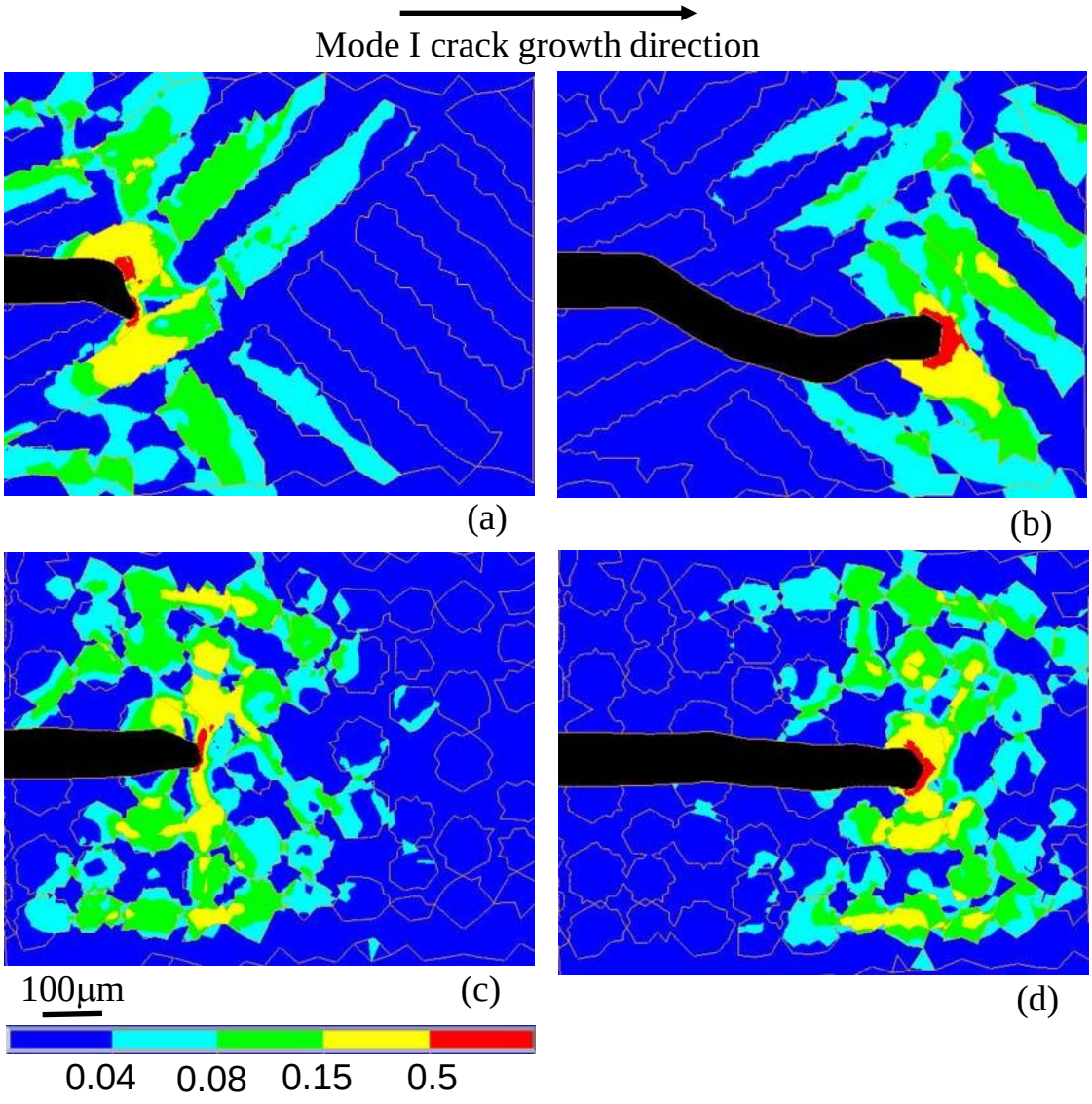

Fig.11 Simulated crack growth paths at two crack lengths, superimposed on equivalent plastic strain contours for models HC (a and b); and RE (c and d). These crack paths corresponds to those paths in Fig. 9.